

## A MESH MORPHING BASED FSI METHOD USED IN AERONAUTICAL OPTIMIZATION APPLICATIONS

M. Andrejašič<sup>1</sup>, D. Eržen<sup>1</sup>, E. Costa<sup>2</sup>, S. Porziani<sup>2</sup>, M. E. Biancolini<sup>3</sup>, and C. Groth<sup>3</sup>

<sup>1</sup> Pipistrel d.o.o. Ajdovščina, R&D, Department of Aerodynamics, Slovenia  
e-mail: matej.andrejasic@pipistrel.si, david.erzen@pipistrel.si

<sup>2</sup> D'Appolonia S.p.A. Italy  
e-mail: emiliano.costa@dappolonia.it, stefano.porziani@dappolonia.it

<sup>3</sup> University of Rome Tor Vergata (UTV), Italy  
e-mail: biancolini@ing.uniroma2.it, corrado.groth@uniroma2.it

**Keywords:** Fluid Structure Interaction, Modal Analysis, Radial Basis Function, Mesh Morphing, Aeronautical Optimization.

**Abstract.** *In this paper a fast and efficient mesh morphing based technique to perform FSI analyses for aeroelastic design and optimization applications is presented. The procedure is based on the finite volume CFD solver (OpenFOAM® and SU2) coupled with the RBF Morph™ tool capable of deforming the surface and volume mesh of the computational domain according to the mode superposition method. Structural vibration modes of the geometry of interest are calculated in a pre-processing stage by means of a FEM solver and later imported into the RBF Morph™ tool to create a set of individual basic deformations. Aerodynamic loads calculated with a CFD solver are then projected onto the accounted structural modes to get modal loads and modal coordinates which are applied to the computational model in order to obtain the deformed configuration. An FSI cycle incorporating a CFD simulation and morphing of its mesh can be iteratively repeated upon convergence to the final deformed shape. Since the modal parameterization and the mesh calculation have to be prepared only once per FSI analysis, its computation time is drastically reduced compared to a standard two-way coupling method in which a structural analysis has to be done at each cycle. Present procedure was applied to two geometries, HIRENASD fuselage-wing geometry for the purpose of testing the procedure and a Pipistrel's electric aircraft propeller for the purpose of optimization of its shape. By utilizing a DoE and a response surface method an increase of four percent of propeller efficiency was obtained by converging to a most favourable propeller pitch and twist configuration incorporating also FSI deformation. The above-mentioned procedure was developed in the framework of the EU-funded RBF4AERO project (Grant Agreement No: 605396) and is available through the RBF4AERO platform.*

## 1 INTRODUCTION

An increasing demand for a faster design phase, optimized final product and reduction of the cost of production in today's world requires a constant development of high fidelity computer-aided engineering (CAE) tools and embedded numerical methods. Multidisciplinary numerical optimization procedures, where multiple physical phenomena are treated at the same time, are therefore desired because they let the engineers to determine their combined effect with a single analysis.

Fluid-structure interaction (FSI) is an example of such multi-physics phenomena where an interaction of a surrounding or internal fluid flow with the movable or deformable structures occurs [1]. FSI is in particular important in aeronautical design, since the safety issue is of the most important concern. All aerodynamic surfaces deform to some extent under aerodynamic forces. Putting aside large scale deformations that cause a malfunction of an airplane, even smaller deformations can cause the airplane to fly at non-optimal configuration. These deformations therefore shouldn't be neglected during the design phase.

In general, all FSI approaches can be grouped according to their governing equations onto monolithic approaches (equations governing the flow and the displacement of the structure are coupled and solved simultaneously) and partitioned approaches (equations are solved separately with two distinct solvers), and according to the treatment of the meshes onto matching and non-matching mesh approaches [2]. For a strong interaction between the fluid and the structure monolithic approaches should be used [3], whereas in cases when the interaction is weak a simpler partitioned approach, with a typical two-way approach example [4], can be used. In order to tackle FSI problems of small deformations the FSI strategy can be simplified even further by incorporating a modal approach and thus avoiding the iteration between the computational fluid dynamics (CFD) and finite element method (FEM) solver [5].

The idea behind the modal approach is that the geometry of interest deforms according to a combination of a limited number of structural mode shapes. FEM calculation therefore has to be performed only once, which leads to a faster overall FSI analysis. Structural deformations are then taken into account directly by morphing the shape of the geometry and the volume mesh surrounding it. Since radial basis functions (RBFs) have been proven in the past as a robust choice for mesh morphing [6-8], they are used as an interpolation basis also in the present work. Morphing is done by exploitation of RBF Morph<sup>TM</sup> software that has been shown as a powerful and effective tool for solving challenging aerospace [9-12] and non-aerospace [13, 14] engineering applications.

A mode-superposition based FSI strategy is presented in this paper. The strategy is applied to a real engineering problem and thus proven as a robust and effective optimization method. The theory behind the modal analysis and RBF-based morphing is presented in Section 2 and 3, respectively. Overall FSI strategy with three distinctive stages is presented in Section 4. The strategy is validated in Section 5 and exploited in an aeronautical optimization application in Section 6.

## 2 MODE-SUPERPOSITION METHOD

Mode-superposition method is a powerful and well-established theory in structural engineering. It is applicable to both free vibration and forced vibration dynamic problems, regardless of the type of the system (continuum or discrete) being treated.

The basic idea of the theory is to use undamped free vibration modes of a structure in order to uncouple the equations of motion. Each vibration mode consists of a natural mode shape, characterizing one of the displacement patterns, and its associated natural frequency. Modal

analysis is therefore a linear theory that enables a determination of the structural static and dynamic response of a discretized system.

The method basically consists of three steps. First, mode shapes and frequencies of a system need to be found performing a modal analysis on the FEM model. The response of each mode under aerodynamic loading is then calculated in the second step. The third step concludes with a superposition of a chosen number of responses to find the full modal response to a given loading.

General equations of motion of an undamped discrete system with  $n$  degrees of freedom (DOF) can be written as

$$\mathbf{M}\ddot{\mathbf{x}} + \mathbf{K}\mathbf{x} = \mathbf{f}(t), \quad (1)$$

where  $\mathbf{x}$  represents a displacement vector,  $\mathbf{M}$  is the mass matrix of the system,  $\mathbf{K}$  is its stiffness matrix and  $\mathbf{f}(t)$  is external excitation vector or loading vector. Assuming an exponential solution  $\mathbf{x} = \mathbf{u} e^{i\omega t}$  Eq. (1) can be rewritten into the following eigenvalue problem [15]

$$\mathbf{K}\mathbf{u} = \omega^2 \mathbf{M}\mathbf{u}, \quad (2)$$

where no external forces were considered. By solving Eq. (2) a complete set of eigenvectors  $\mathbf{u}$ , that represent mode shapes, and eigenvalues  $\omega^2$ , that lead to natural frequencies  $\nu$  as  $\omega = 2\pi\nu$ , for all DOF can be obtained. Eq. (2) therefore states that a vibration mode is a configuration in which a balance between elastic resistance and inertial loads occurs.

According to the eigendecomposition operation all eigenvectors, i.e. mode shapes, are orthogonal and form a basis of the eigenvalue problem [16]. The dynamic response of a mechanical system can therefore be represented by a superposition of all mode shapes as

$$\mathbf{x} = \mathbf{U}\boldsymbol{\eta}, \quad (3)$$

where matrix  $\mathbf{U}$  and vector  $\boldsymbol{\eta}$  represent a complete set of modal shapes and modal coordinates, respectively. Mode superposition is therefore a weighted sum of all mode shapes, where modal coordinates represent the weights.

A convenient normalization can be obtained by imposing a unit modal mass for each mode shape  $\mathbf{u}_m$ , which, taking into account also the orthogonality of the basis, results into

$$\mathbf{u}_m^T \mathbf{M} \mathbf{u}_m = 1, \quad m = 1, 2, \dots, n. \quad (4)$$

By inserting Eq. (4) into Eq. (2) an additional simplification can be obtained as

$$\mathbf{u}_m^T \mathbf{K} \mathbf{u}_m = \omega_m^2. \quad (5)$$

Equations of motion (Eq. (1)) can be, using Eqs. (3), (4) and (5), finally rewritten into  $n$  uncoupled and independent single DOF systems [17]

$$\ddot{\eta}_m + \omega_m^2 \eta_m = \mathbf{u}_m^T \mathbf{f}(t) \quad (6)$$

that can be solved one at the time in order to obtain all needed modal coordinates  $\eta_m$ . Each nodal force defined as

$$N_m(t) = \mathbf{u}_m^T \mathbf{f}(t) \quad (7)$$

can be therefore obtained by multiplying mode eigenvector  $\mathbf{u}_m^T$  by a real physical force distribution  $\mathbf{f}(t)$ . The complete response of a system to a given loading can finally be obtained using Eq. (3), with all entities known.

The number of mode shapes of a structure is in reality equal to its total number of DOF, i.e. infinite for a continuum system. In practice it is not necessary to employ all mode shapes in order to describe the system. Since the energy associated with each mode decreases with in-

creasing frequency, a good approximation can be obtained by superimposing only first few most energetic mode shapes  $n_{modes}$  that tend to provide the greatest contribution to structural response [15].

Modal approach is typically exploited in dynamic analyses in which the number of modes retained is defined on the basis of excited frequencies. Nevertheless, it can be used even for approximating a static solution. In this case, Eq. (6) can be simplified to

$$\omega_m^2 \eta_m = N_m. \quad (8)$$

### 3 RBF-BASED MORPHING

Proposed FSI strategy employs mesh morphing done in RBF Morph<sup>TM</sup> tool. The morphing is based on the RBFs defined at discrete points (source points) that are in this way able to interpolate an  $n$  dimensional scattered data. The interpolation ensures a smooth morphing of the computational CFD mesh and at the same time, an exactly prescribed displacement of the source points.

After defining a set of source points, whether on the surface of the geometry of interest or in the volume space surrounding it, with their displacement, the solution of the RBF mathematical problem is sought by the computation of the scalar parameters of a linear system of the order equal to the number of considered source points. Once the RBF system coefficients have been computed, the displacement of an arbitrary node of the mesh, either inside or outside of the domain, can be expressed as a sum of the radial contribution of each source point. In such a way, a desired modification of the mesh nodes position can be rapidly applied preserving mesh topology.

RBFs can be classified on the basis of the type of the support (global or compact) they have, meaning the domain where the chosen RBF is non zero-valued. The behaviour and the quality of the interpolation therefore depend on the chosen RBF.

An interpolation function composed of an RBF  $\varphi$  and a polynomial  $H$  of order  $h - 1$  ( $h$  is the order of  $\varphi$ ), introduced with the aim to guarantee the compatibility with the rigid motion, is defined as

$$I(\mathbf{r}) = \sum_{i=1}^S \gamma_i \varphi(\|\mathbf{r} - \mathbf{r}_{k_i}\|) + H(\mathbf{r}), \quad (9)$$

where  $\mathbf{r}$  is a vector identifying the position of a generic node belonging to the surface or volume mesh,  $\mathbf{r}_{k_i}$  is the  $i$ -th source point position vector ( $S$  is their total number) and  $\|\cdot\|$  is the Euclidean norm, namely the distance between two points. The minimal degree of polynomial  $H$  depends on the choice of the RBF. A unique interpolant exists if the RBF is conditionally positive definite function [18]. In that case a linear polynomial

$$H(\mathbf{r}) = \beta_1 + \beta_2 x + \beta_3 y + \beta_4 z \quad (10)$$

can be used with RBFs of order  $h \leq 2$  [19]. A radial basis fit exists if the coefficients  $\gamma_i$  of the RBF and the weights of the linear polynomial vector  $\beta_i$  can be found such that the desired values of displacement  $g_i$  are obtained at source points and the polynomial terms give no contributions at source points, i.e.

$$I(\mathbf{r}_{k_i}) = g_i, 1 \leq i \leq S; \quad \sum_{i=1}^S \gamma_i q(\mathbf{r}_{k_i}) = 0 \quad (11)$$

for all polynomials  $q$  with a degree less or equal to that of polynomial  $H$ . Coefficients  $\gamma_i$  and  $\beta_i$  can be obtained by solving the system

$$\begin{pmatrix} \mathbf{R} & \mathbf{P} \\ \mathbf{P}^T & \mathbf{0} \end{pmatrix} \begin{pmatrix} \gamma \\ \beta \end{pmatrix} = \begin{pmatrix} \mathbf{g} \\ \mathbf{0} \end{pmatrix}, \quad (12)$$

where  $\mathbf{R}$  is the interpolation matrix defined by calculating all the radial interactions between source points

$$R_{ij} = \varphi \left( \left\| \mathbf{r}_{k_i} - \mathbf{r}_{k_j} \right\| \right), \quad 1 \leq i \leq S, 1 \leq j \leq S \quad (13)$$

and  $\mathbf{P}$  is a constraint matrix that arises to balance the polynomial contribution and contains a column of "1" and the  $x, y, z$  positions of the source points in the other three columns

$$\mathbf{P} = \begin{pmatrix} 1 & x_{k_1} & y_{k_1} & z_{k_1} \\ 1 & x_{k_2} & y_{k_2} & z_{k_2} \\ \vdots & \vdots & \vdots & \vdots \\ 1 & x_{k_N} & y_{k_N} & z_{k_N} \end{pmatrix}. \quad (14)$$

RBF interpolation works for scalar fields, hence a system of the form of Eq. (12) has to be solved for each of the three spatial directions.

Using RBF method for interpolation purposes has several advantages that makes it very attractive for mesh morphing. Since it is a meshless method only grid points are moved regardless of the type of the volume cells they belong to. This makes the method suitable for parallel implementation that can potentially handle meshes with large number of cells [20]. In fact, once the solution is known and shared in the memory, each computer core has the ability to morph the nodes on its own mesh partition without knowing what is happening outside. The reason for that lies in a global range of the interpolation function where the continuity at interfaces is implicitly guaranteed. The method is, in spite of its meshless nature, able to exactly prescribe desired deformations of the geometry of interest. This is achieved by using all the surface mesh nodes as RBF source points with prescribed displacements, including the simple zero displacement condition at the surface that should be left by the morphing tool as undeformed.

#### 4 FSI STRATEGY

FSI strategy proposed in the present paper is composed out of three sequential stages: vibration modes calculation, RBF solution generation using RBF Morph<sup>TM</sup> tool and at the end an iterative FSI cycle employing CFD solver and mesh morphing through RBF solutions.

At the first stage, structural mode shapes and associated natural frequencies of deformable parts, that are utilized in the mode superposition phase, are calculated by means of a FEM solver. For the present paper, Ansys<sup>®</sup> APDL solver was used in the validation test case (Section 5), whereas Abaqus<sup>TM</sup> FEA software was adopted in the propeller optimization test case (Section 6). The number of physically most prominent mode shapes that are used in the subsequent stages has to be chosen at this point. It should be mentioned here that the FEM mesh doesn't have to be conformal to the CFD mesh (used at the third stage) at the geometry surface. For a typical industrial problem, CFD simulation needs a few times finer mesh at the surface (in order to simulate or model boundary layer effects) compared to the mesh used at the FEM calculation. FEM mesh nodes therefore in general don't coincide with CFD nodes. Because of this reason an interpolation step between both meshes is introduced at the third stage that leads to as universal FSI strategy as possible.

RBF solution for each mode shape is calculated at the second stage. This is done by the means of the deformable surface displacement distribution of the corresponding mode shape obtained in previous stage. Parts of the geometry that are considered as rigid are kept constrained. In order to obtain an adequate level of CFD mesh quality after each FSI cycle morphing iteration, a special attention should be given to each RBF solution. For this reason a proper source point's density and morphing domain dimensions should be used.

The third stage of the proposed strategy employs an FSI cycle composed out of CFD simulation, modal coordinates calculation and mesh morphing steps. FSI cycle is basically an iterative process which deforms the baseline geometry in such a way that the internal tension forces of the structure counteracts the aerodynamic loads on the geometry surface. Since it is an iterative process the cycle is finished when the resultant force on the surface converges below a certain threshold, defined by the user.

A surface distribution of aerodynamic forces  $\mathbf{f}$  that act on the geometry of interest, as a consequence of the airflow passing by, is calculated via a CFD simulation. This aerodynamic load, comprised out of two contributions (pressure force and viscous force), deforms the geometry. In order to apply the deformation in a modal space, a modal force for each mode  $m$  can be calculated using Eq. (7) as

$$N_m = \sum_{i=1}^{n_{surf}} \mathbf{u}_{m_i}^T \mathbf{f}_i. \quad (15)$$

Each modal force is therefore a scalar obtained by integrating the external load field over the entire structure (all surface nodes) weighted by the  $m$ -th mode eigenvector. According to Eq. (8) each modal coordinate can then be calculated as

$$\eta_m = \frac{N_m}{\omega_m^2}. \quad (16)$$

The last step of the FSI cycle represents the morphing of the mesh and the geometry. A linear superposition of all chosen mode shapes (RBF solutions) weighted by the modal coordinates is applied to the CFD mesh in order to deform it. This crucial step is in the modal space represented by the following relation

$$\mathbf{r}_{CFD} = \mathbf{r}_{CFD_0} + \sum_{m=1}^{n_{modes}} \eta_m \mathbf{u}_m, \quad (17)$$

where  $\mathbf{r}_{CFD_0}$  and  $\mathbf{r}_{CFD}$  represent the position of CFD mesh nodes before and after the deformation, respectively. As a consequence of this very same geometry deformation, the aerodynamic loads are altered at the same time. Next FSI cycle iteration therefore requires another CFD simulation on altered geometry that calculates new force distribution and the FSI cycle can continue upon convergence. The proposed FSI approach bypasses several complexities related to the implementation of the alternative two-way FSI procedures. Its advantage is that after the first stage, no further iteration with the structural solver is required, which drastically reduces the time of the analysis.

## 5 HIRENASD TEST CASE

A model employed to accomplish a validation of the present FSI approach is one of the configurations supplied at the 1<sup>st</sup> Aeroelastic Prediction Workshop (AePW) [21] launched by NASA. In particular, the wind tunnel model of this HIgh REynolds Number Aero-Structural

Dynamics (HIRENASD) configuration [22] tested in the Cologne European Transonic Wind tunnel (Figure 1), consists of a tapered  $34^\circ$  aft-swept wing with a BAC3-11/RES/30/21 supercritical airfoil profile and a wing span of 1.286m. The numerical and experimental investigations of the test case have been performed under  $Mach = 0.8$ ,  $Re = 7 \cdot 10^6$  (based on the 0.345m reference wing root chord), air density  $\rho = 1.22\text{kg/m}^3$  and angle of attack (AoA) =  $1.5^\circ$  flow conditions (ETW132 data point [22]).



Figure 1: HIRENASD wind tunnel model.

### 5.1 Mode shapes and RBF solutions

Mode shapes and natural frequencies have been calculated using the ANSYS® APDL solver from the FEM model, consisted of the wing, the excitation system and the balance, in NASTRAN format made available by the AePW committee [21]. For the FSI analysis the first six vibration modes were chosen; their shapes, together with the corresponding natural frequencies, are depicted in Fig. 2, starting with Mode 1 at the top left and ending with Mode 6 at the bottom right. According to the AePW classification, label B is assigned to the out-of-plane bending and label Fa to the in-plane fore-and-aft bending.

In the second stage, an RBF solution has been generated for each of the six modes through the RBF Morph™ tool. Since in both the wind tunnel and the FEM model the fuselage aerodynamic fairing is mechanically uncoupled from the wing root, a slight deformation of the fairing is allowed. This is achieved by removing fixed source points from the portion of the fuselage near the wing root (Fig. 3 left) leaving the rest of the fuselage undeformable. Additional box-shaped encapsulation domain, presented in Fig. 3 right, is utilized to limit the morphing action to the CFD mesh volume close to the HIRENASD geometry.

### 5.2 FSI cycle

FSI analysis was divided in two subsequent simulation phases that ran on a mixed 1.5 million cell SOLAR unstructured grid made available by the AePW committee [21]. Both phases employed a steady CFD simulation using a compressible flow SU2 solver with a low-Reynolds Spalart-Allmaras turbulence model. A fully developed airflow passing a stiff geometry (baseline) was obtained in the first phase, whereas the elastic behaviour of the geometry was taken into account in the second phase through the FSI cycle described in the Section 4. Since the baseline flow field is not far from the final deformed one, the proposed two-phase approach accelerated the FSI cycle convergence through smaller number of CFD iterations in the second phase. Aerodynamic load distribution, integrated to obtain all modal forces

through Eq. (15), was composed only out of pressure force contribution. Shear stresses were neglected.

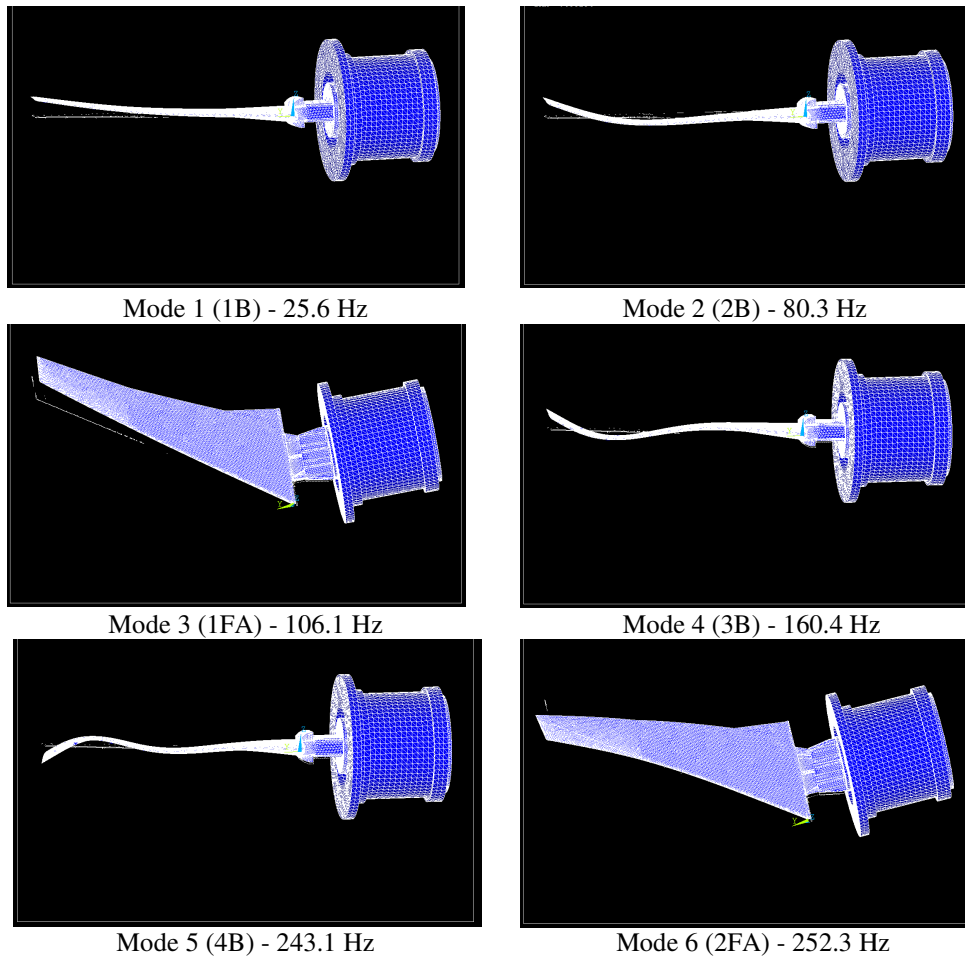


Figure 2: First six mode shapes and natural frequencies of the HIRENASD model.

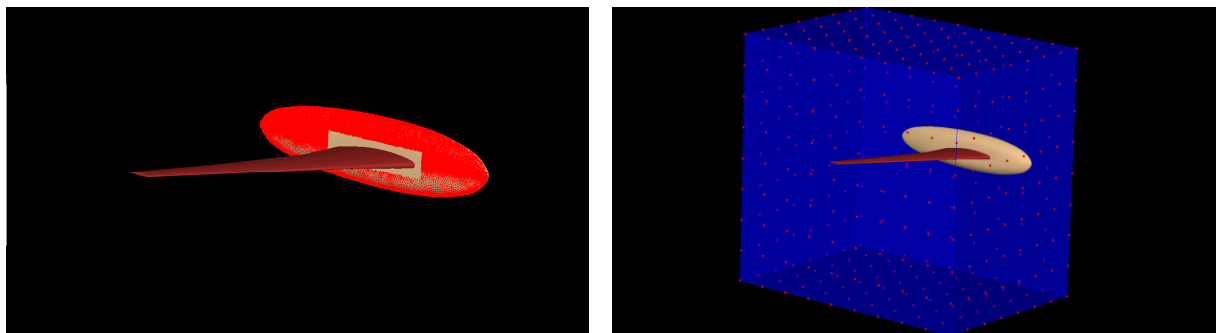


Figure 3: Fixed (left) and encap domain (right) source points.

The surface pressure distribution for the baseline configuration is visualised in Fig. 4 left, with the position of the shock wave quickly noticeable along the wing span. The  $y^+$  surface distribution with values under 1, can be seen in Fig. 4 right.

The validation of the proposed FSI strategy was performed by comparing three different calculation outputs with respect to either numerical or experimental data, which can be found in [23]. The first output was the vertical displacement of the wing tip of the fully converged wing (deformed) with respect to the baseline. A comparison of the baseline geometry (grey

colour at the bottom) and the deformed one (green colour on top) can be seen in Fig. 5 left. A zoom-in on the wing tip is added in order to easily compare its position at different FSI cycle iterations. As the wing's shape of the third and fourth cycle almost coincides, the convergence of the static aeroelastic solution can be judged as reached. The convergence of the vertical displacement value at the trailing edge wing tip point during the FSI study is depicted in Figure 5 right. The converged value is 14.60 mm, which is very close to the numerical results found in [23] for two different grid setups (13.74 mm for Grid A and 14.02 mm for Grid B).

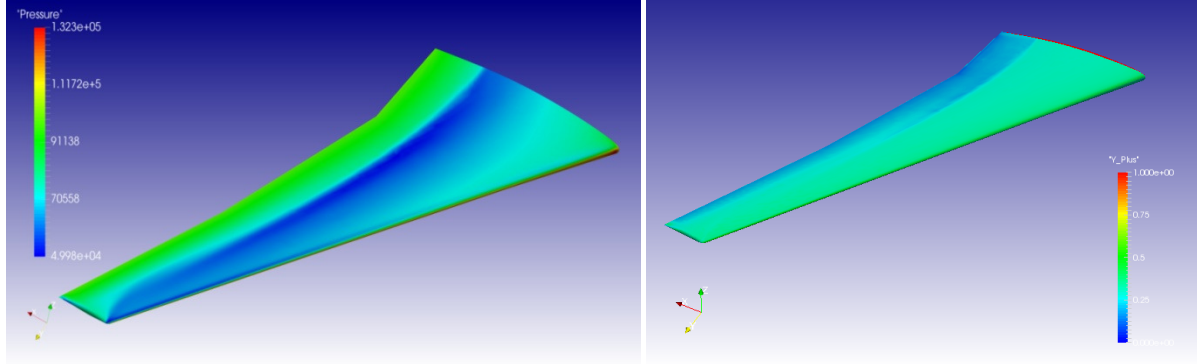


Figure 4: Steady state pressure (left) and  $y^+$  (right) distribution on the HIRENASD baseline configuration.

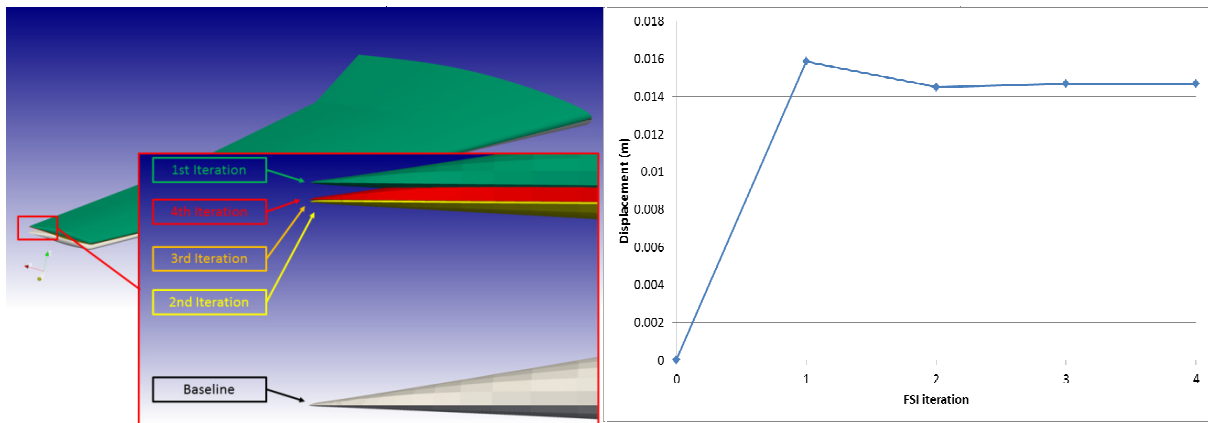


Figure 5: Comparison of wing baseline (grey) and its deformed geometry (green) together with a wing tip zoom-in detail (left). Wing tip vertical displacement at consecutive FSI cycle iterations (right).

The second FSI strategy validation was performed by comparing the pressure coefficient distribution with respect to the experimental data presented in [23] for a deformed geometry. The comparison at four different wing-span locations (in percentage of the wing span  $b$ ) is depicted in Fig. 6. Even though some deviations of the numerical results from the experimental measurements can be observed on the pressure suction side the comparison can be still treated as satisfactory.

Furthermore, a good agreement between the proposed approach and the literature numerical results [23] of the lift and the drag aerodynamic coefficients for the baseline and the deformed geometry can be observed in Table 1. The results also show a strong influence of the deformation at both lift and drag coefficient. Based on the presented results of all three validation criteria the proposed FSI strategy validation can be considered as positively accomplished.

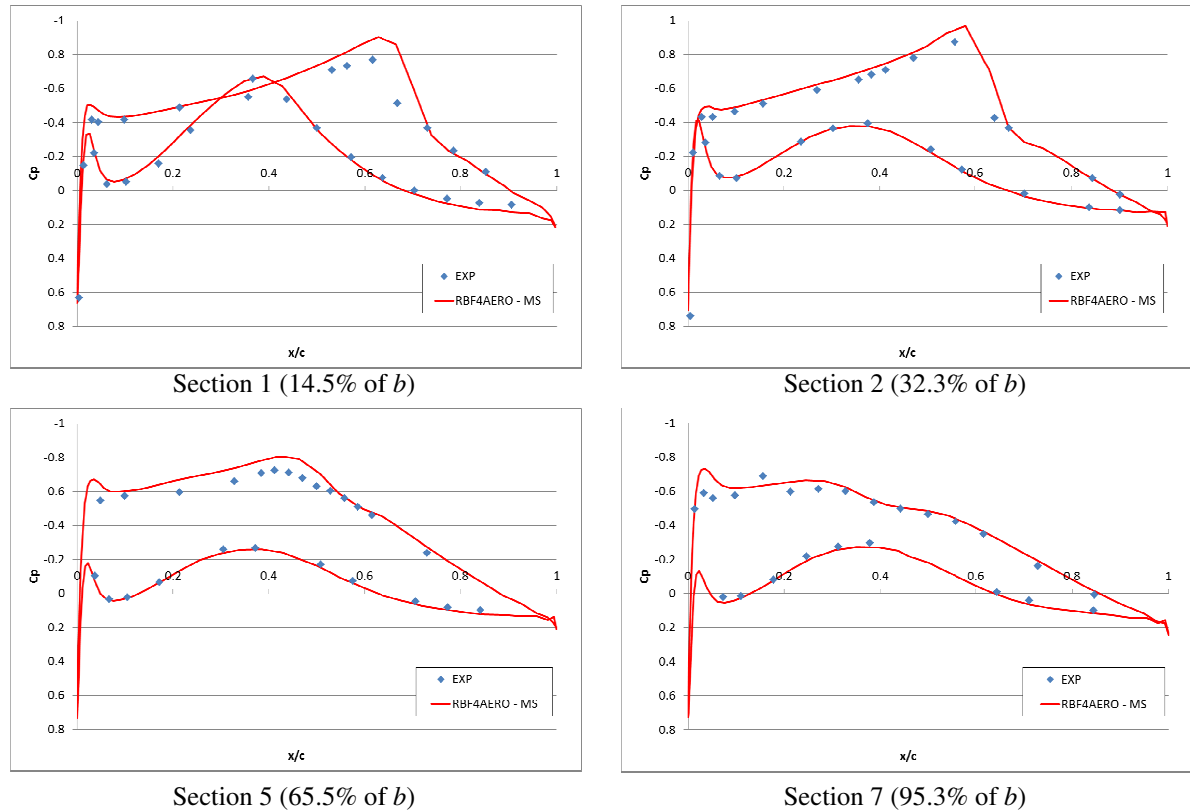


Figure 6: Comparison of numerical (RBF4AERO-MS) and experimental (EXP) pressure distribution at four different wing section locations.

Aerodynamic coefficient	Baseline			Deformed		
	Proposed approach	Grid A (NASA)	Grid B (NASA)	Proposed approach	Grid A (NASA)	Grid B (NASA)
$C_l$	0.3593	0.3542	0.3544	0.3407	0.3373	0.3366
$C_d$	0.0151	0.0173	0.0154	0.0144	0.0166	0.0147

Table 1: Aerodynamic coefficients comparison between the proposed approach and documented numerical results for two different grid set-ups [23] for the baseline and the deformed geometry.

## 6 PROPELLER OPTIMIZATION

In this case, spinning aircraft propeller deformations due to aerodynamic loads are investigated. As a consequence of the deformation propeller's aerodynamic characteristics change with respect to the ones calculated on the initial geometry. Since the power needed to spin the propeller and the thrust the propeller is capable of differ from the expected ones, the propeller designer must take into account such deformations. The objective of the present test case was to increase the efficiency of the chosen propeller taking into account its deformed shape by means of the proposed FSI strategy through design of experiments (DoE) analysis.

Test case employs a two-bladed fixed pitch propeller measuring 1.6m in diameter (Fig. 7 left). The propeller is a result of an in-house design and it is intended for a particular Pipistrel's electric aircraft - WATTsUP (Fig. 7 right). In order to simplify the analysis only a spinner, extended into a water drop like shape, was used substituting the complete aircraft. All CFD simulations including the calculations of the aerodynamic loads were done using finite

volume open source software OpenFOAM® where a multi reference frame (MRF) approach was used. In this way an absolute velocity field is calculated in a rotating frame of reference and the problem reduces to a steady-state calculation. With introduction of cyclic boundary conditions only a half of the propeller had to be simulated, which simplified the problem even further.

The mesh, prepared by the snappyHexMesh utility, consists of 1.6 million cells in a cylindrical volume domain (Fig. 8 left). MRF zone occupies only a small portion of the complete volume and with its cylindrical shape it tightly embraces the propeller and the spinner (Fig. 8 right). The propeller has been simulated and later optimized in a take-off and cruise flight regimes. During take-off the propeller spins at 2300RPM and the inflow velocity is 30m/s, which results in a tip Mach number of 0.57. During cruise on the other hand the propeller spins at 2550RPM. The inflow velocity is 51.4m/s which results in a tip Mach number of 0.65. Even though the Mach numbers are quite high the effects of compressibility were not taken into consideration in order to simplify the CFD simulation. Instead an incompressible RANS solver simpleFoam was used employing high-turbulence Spalart-Allmaras turbulence model. Densities of  $1.19\text{kg/m}^3$  and  $1.11\text{kg/m}^3$ , and kinematic viscosities of  $1.5 \cdot 10^{-5} \text{ m}^2/\text{s}$  and  $1.58 \cdot 10^{-5} \text{ m}^2/\text{s}$  were used as airflow properties at the take-off and cruise simulations, respectively.  $y^+$  and pressure surface distributions of a converged baseline simulation at take-off condition can be seen in Fig. 9.  $y^+$  ranges on average from a value of 10 to a satisfactory maximum of 130.

According to the CFD simulation the propeller baseline produces approximately 1070 N of thrust force and needs 53511 W of power in order to overcome the aerodynamic drag.

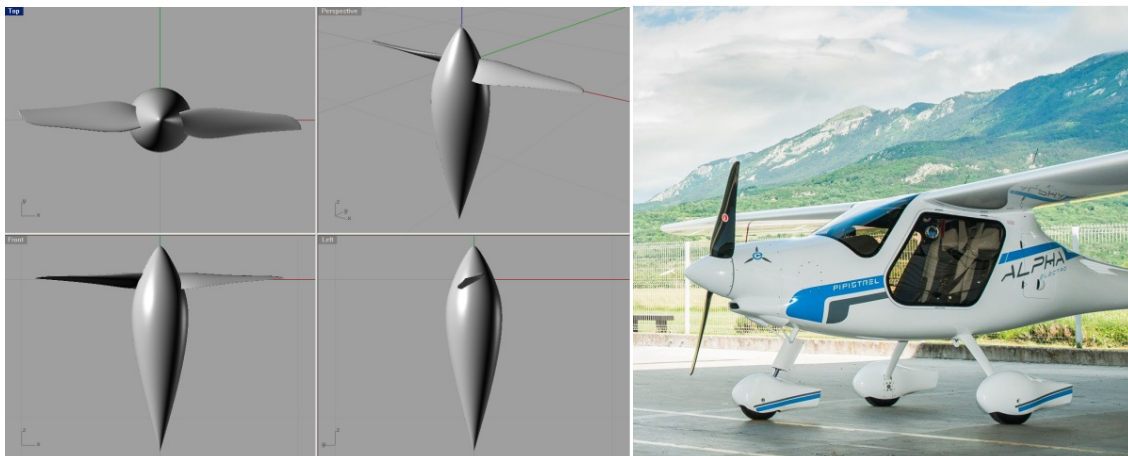


Figure 7: CAD model of the propeller geometry (left), physical propeller mounted on Pipistrel's electric aircraft – WATTsUP (right).

## 6.1 Mode shapes and RBF solutions

The propeller with its internal structure was analyzed with the Abaqus™ FEA software where its mode shapes and natural frequencies were calculated in a rotated frame of reference. A subset of first five physically most prominent modes has been chosen for the mode-superposition FSI approach. Emphasized mode shapes together with the corresponding frequencies are presented in Fig. 10, starting with Mode 1 at the top left and ending with Mode 5 at the bottom right. First four modes represent first four bending deformation modes, whereas the fifth mode represents the first order of twist deformation.

Individual eigenvectors are then used as inputs for the RBF Morph™ tool where RBF solutions for the CFD mesh morphing are computed. In order to reduce the morphing time, a morphing domain is set in a form of a cylinder around the propeller blade (Fig. 11). Mesh

morphing is therefore limited only to this domain volume thus leaving the major portion of the CFD mesh undeformed. Since the propeller is mechanically not connected to the spinner, a small portion of the spinner around the propeller root is allowed to modify, leaving most of the spinner undeformed.

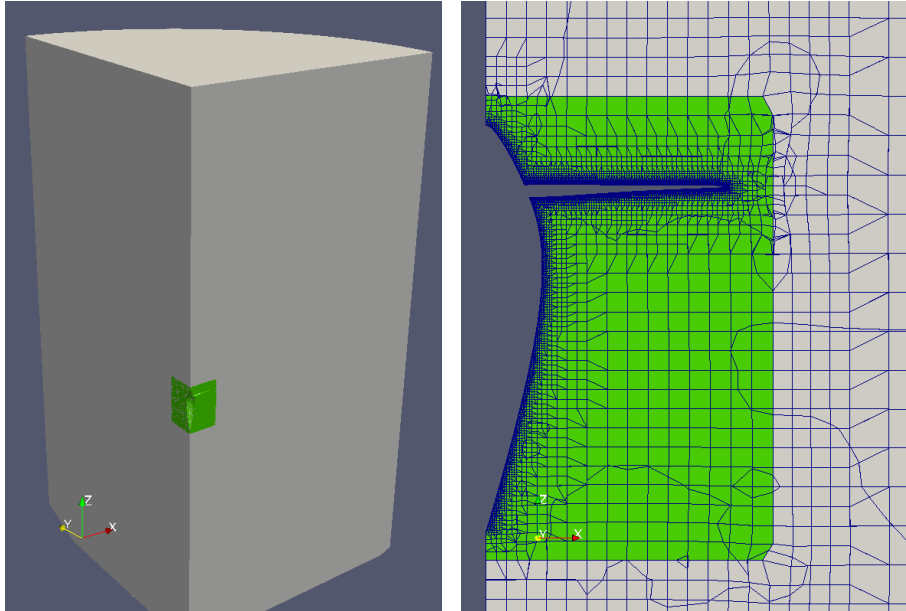


Figure 8: A half of the total CFD volume mesh (left) and a slice through a mesh (right). MRF zone is denoted in green colour.

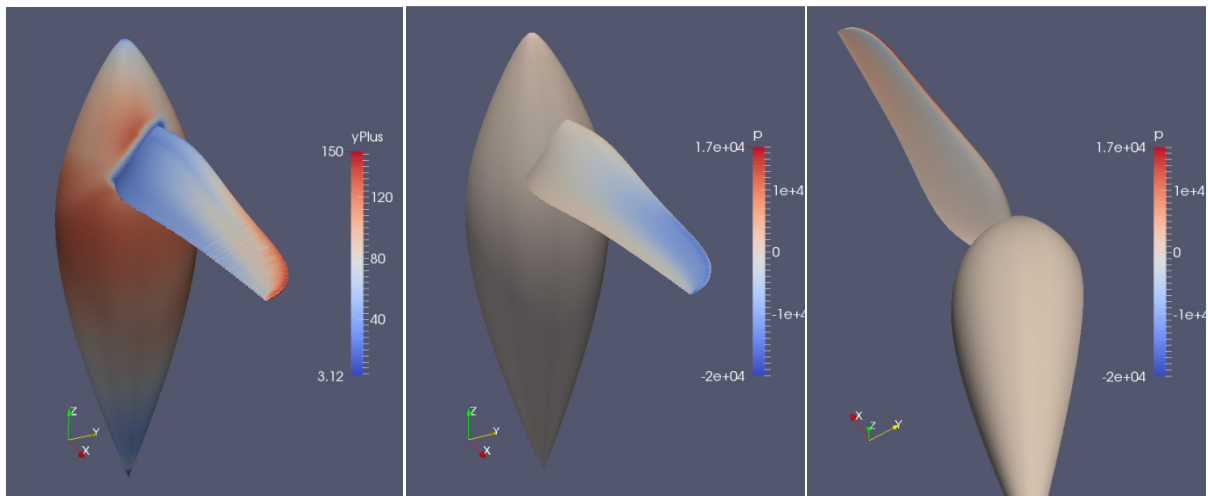


Figure 9:  $y^+$  (left) and pressure surface distribution on the upper (middle) and bottom (right) side of a fully converged baseline simulation at take-off flight conditions.

## 6.2 FSI baseline results

First an FSI analysis was run on propeller baseline geometry at take-off conditions. An absolute value of a relative difference of each modal coordinate with respect to its converged value (fifth iteration) over first four FSI cycle iterations is depicted in Fig. 12 left. All modal coordinates vary for less than 0.2% already after the second iteration. Other representatives of fast convergence of proposed FSI strategy are the characteristic properties of the propeller, thrust and power, collected at each iteration (Fig. 12 right). Here, the left and the right ordi-

nate axes represent propeller thrust in Newtons and its power in Watts, respectively. It can be seen that both propeller characteristics practically don't change after the second iteration.

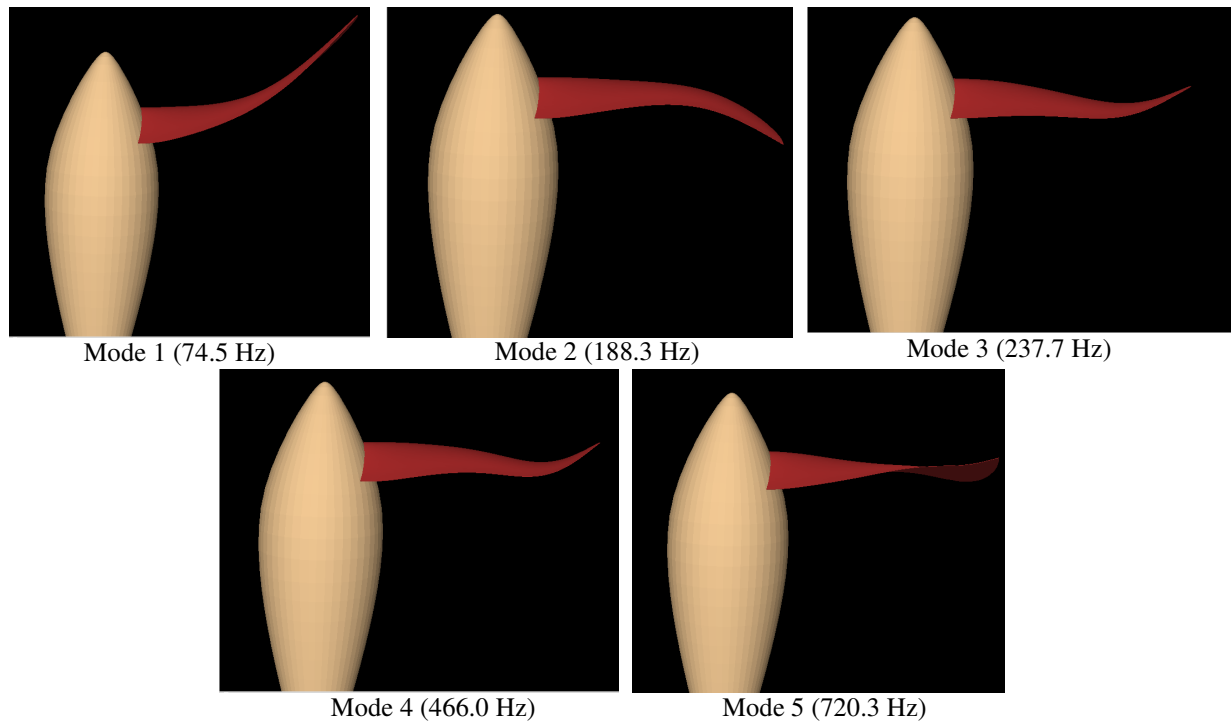


Figure 10: First five propeller blade mode shapes with corresponding natural frequencies. Amplitudes are emphasized for better presentation.

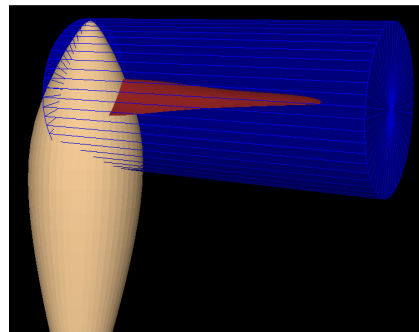


Figure 11: Morphing domain around the propeller blade depicted in blue colour.

Deformation of the propeller geometry during the FSI analysis can be observed in Fig. 13. Geometry comparison was done in software ParaView. The baseline geometry is depicted in grey colour, the first FSI iteration in green colour and the fifth FSI iteration (final and converged geometry) in red colour. The most obvious deformation is blade root bending being also the first and also the most dominant eigenmode. Such deformation results as a consequence of the large suction region (low pressure) on the outer portion of upper side of the blade seen in the middle Fig. 9. Slight blade tip twist can also be noticed in Fig. 13. The source of such deformation can be assigned to the high pressure region located on the outer and aft portion of lower side of the blade seen on the right hand side of Fig. 9.

Results of the FSI analysis on the baseline configuration at the take-off conditions and at cruise conditions are presented in numbers in Table 2 and Table 3, respectively. From both tables it can be seen that the thrust and the power do not change significantly in spite of a

quite perceivable geometry change between the baseline and the deformed geometry. Convergence of all modal weights, propeller thrust and power (Fig. 12) as well as the geometry deformation (Fig. 13) indicate a very rapid FSI procedure converge which drastically accelerated the optimization presented in the following section.

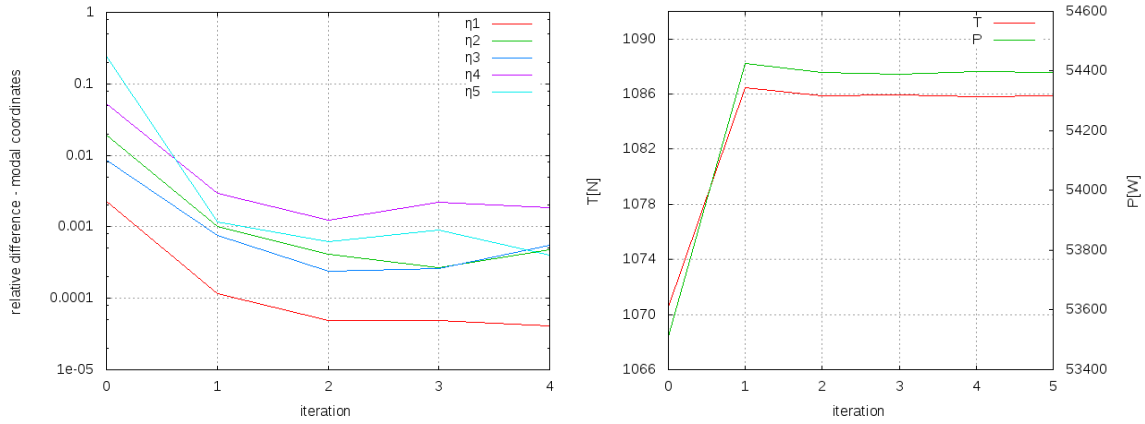


Figure 12: Convergence of a relative difference (absolute value) of each modal coordinate (with respect to its converged value) (left) and propeller thrust and power (right) during FSI analysis for the propeller baseline at take-off conditions.

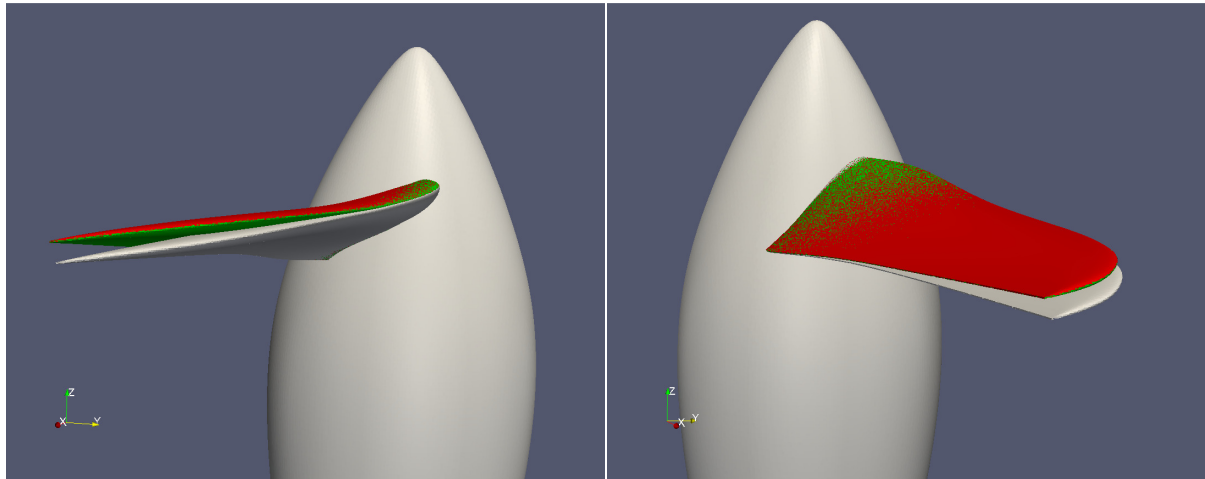


Figure 13: Comparison of propeller blade geometry at different FSI iterations at take-off flight conditions. Baseline (grey), the first iteration (green) and the fifth and final iteration (red).

Parameter	0. iteration/baseline	5. iteration	relative difference
Thrust force (N)	1070	1086	+1.5%
Power (W)	53511	54395	+1.6%

Table 2: Results of an FSI analysis on baseline configuration at take-off conditions.

Parameter	0. iteration/baseline	5. iteration	relative difference
Thrust force (N)	223	220	-1.4%
Power (W)	28941	28820	-0.4%

Table 3: Results of an FSI analysis on baseline configuration at cruise conditions.

### 6.3 Propeller optimization

The main objective of the present test case, propeller optimization, was met through DoE analysis employing proposed FSI strategy. Optimization variables, chosen to find the optimal propeller geometry in the vicinity of the baseline shape, were propeller pitch  $p$  and twist angle  $t$ . Both deformations were applied using RBF Morph<sup>TM</sup> tool. As a result, no additional meshing was needed in order to run CFD simulations. Propeller was optimized with respect to two flight regimes (take-off and cruise conditions) for as large propeller efficiency as possible. The optimization objective function used was a weighted sum of propeller efficiencies at cruise and take-off flight condition

$$F(t, p) = \frac{1}{2} v_{CRUISE} + \frac{1}{2} v_{TAKE-OFF}, \quad (18)$$

with the propeller efficiency defined as

$$\eta = \frac{TV}{P}, \quad (19)$$

where  $V$  denotes the velocity of the aircraft (cruise or take-off). As it can be seen from Eq. (18), both contributions were equally weighted. By varying optimization variables, propeller pitch and twist angle, a maximal combined efficiency and therefore an optimal propeller geometry was sought. A positive pitch angle change is defined as an increase of the angle of attack of the airflow incidenting on the propeller blade (Fig. 14 left). Positive twist angle on the other hand reduces the local pitch angle of attack (Fig. 14 middle).

Pitch and twist variations were introduced to the geometry via morphing procedure by applying additional artificial morphing RBF solutions at the morphing step of the FSI cycle. Since the fifth propeller mode shape represents a twist-like deformation by itself, the said mode was used to apply the additional twist to the propeller shape. On the other hand, the pitch variation had to be applied by calculating additional RBF solution. For the latter, a new moving domain in a shape of a cylinder and a bigger morphing domain were set (Fig. 14 right). All mesh cells, located inside the moving domain (red), rotated around the blade spanwise axis for a prescribed pitch angle. The cells embraced in the morphing domain (blue), but located outside of the moving domain, were morphed in such a way that a smooth transition from rotated to stationary cells (outside of the morphing domain) was made. At this point an assumption has been made that the change of mode shapes and natural frequencies caused by the deformation (of small extend) of the geometry (pitch and twist angle) is negligible.

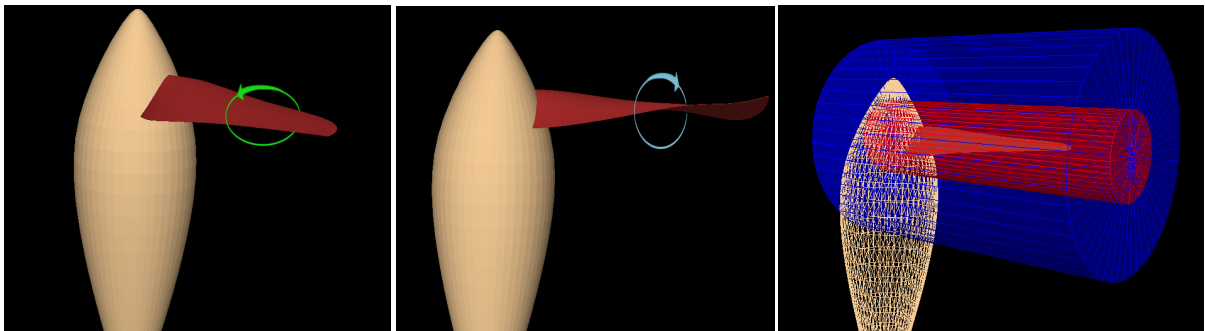


Figure 14: The pitch (left) and twist (middle) positive direction deformation indicated by an arrow. The morphing domain (blue cylinder) and the moving domain (red cylinder) (right).

At each of two flight conditions a separate DoE table was filled with 8 times 9 different combinations of pitch and twist deformations around the baseline configuration. Each point in

the DoE table is calculated using a proposed FSI cycle strategy, combining CFD simulations and mesh morphing. The whole procedure was performed automatically using bash script. The script chose a combination of the optimization parameters, started FSI cycle and stored the results for each set of parameters. The results of both DoE procedures are presented in Fig. 15. Each blue dot represents a single DoE point, where the efficiency is calculated from the thrust and power of the deformed propeller geometry.

DoE results were in a postprocessing phase interpolated using a third degree polynomial surface (coloured surfaces in Fig 15). A summation of both surfaces according to Eq. (18) formed a surrogate model that was later used in order to perform a constrained optimization. Constraints used were take-off and cruise engine power i.e. 55 kW and 41.3 kW, respectively. The output of the optimization was a pitch and twist pair ( $p, t$ ), that produced the maximal objective function i.e. the maximal weighted sum of both efficiencies. Surrogate model is together with the baseline configuration (green point) and optimal configuration (blue point) presented in Fig. 16.

Pitch and twist angles in the optimal point are  $1.045^\circ$  and  $1.482^\circ$ , respectively. The weighted sum of both efficiencies increased by 4.0%. Taking into account the fact that only two global degrees of freedom were used in order to optimize the propeller and that the baseline geometry already presents an optimized design (done in the past by other Pipistrel in-house software), such an increase of efficiency can be considered as a satisfactory result.

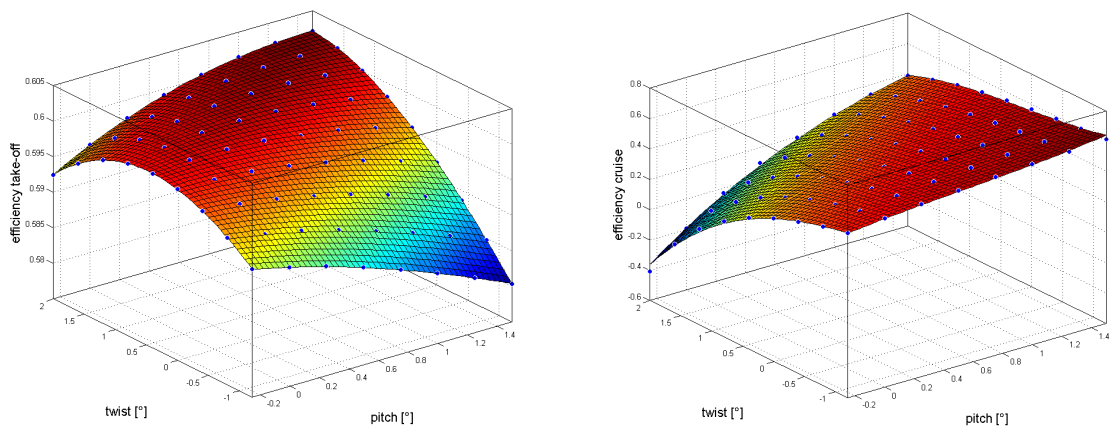


Figure 15: DoE results at 72 different pitch and twist pairs for take-off (left) and cruise (right) flight conditions.

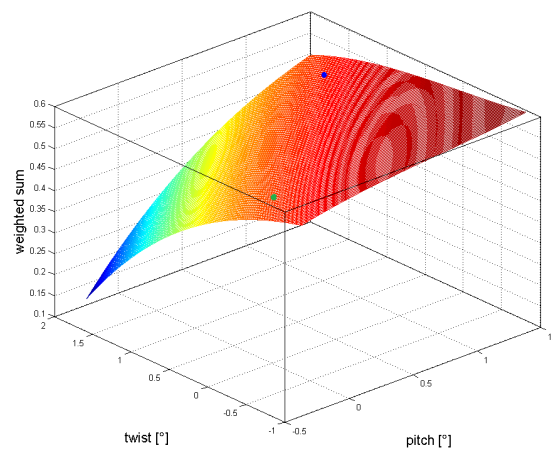


Figure 16: Surrogate model with the baseline configuration denoted with a green point and optimal configuration with blue point.

A comparison of the deformed optimized (red) and the deformed baseline geometry (grey) can be seen in Fig. 17. From the figure it can be seen how did the local angle of attack at the blade inner section increase by the positive pitch angle yet decrease at the blade outer section by the positive twist angle. Thrust force and power of the optimized propeller are for the baseline (0th iteration) and deformed configuration (5<sup>th</sup> iteration), together with their relative difference, presented in Table 4 for the take-off flight condition and in Table 5 for the cruise condition. The order of magnitude of relative differences didn't change from the baseline analysis (Tables 1 and 2).

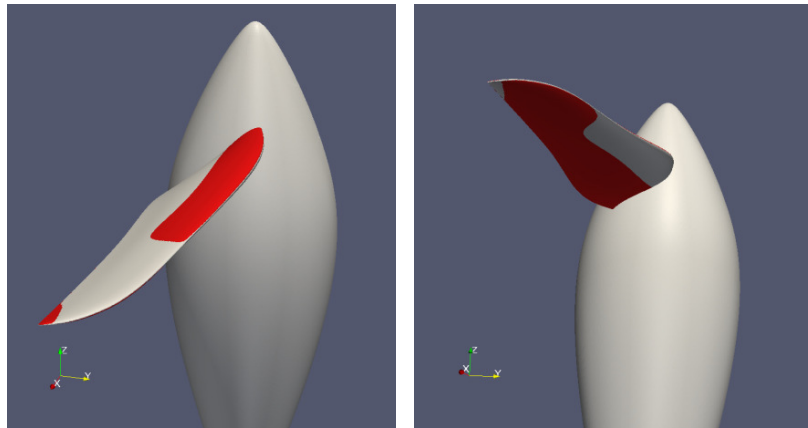


Figure 17: Geometry comparison of deformed optimized propeller blade (red) and deformed baseline configuration (grey).

Parameter	0. iteration/baseline	5. iteration	relative difference
Thrust force (N)	1089	1102	+1.2%
Power (W)	54140	55004	+1.6%

Table 4: Main results of the FSI analysis at optimal pitch and twist at take-off conditions.

Parameter	0. iteration/baseline	5. iteration	relative difference
Thrust force (N)	251.2	247.4	-1.5%
Power (W)	30049	29901	-0.5%

Table 5: Main results of the FSI analysis at optimal pitch and twist at cruise conditions.

## 7 CONCLUSIONS

A mesh morphing based FSI strategy was proposed that, connecting the modal analysis of the structure of interest, transformation of calculated mode shapes directly to the CFD environment using radial basis functions, and iterative calculation of aerodynamic loads and CFD mesh morphing, presents an efficient and reliable analysis of engineering problems.

FSI strategy was first validated by analyzing a well-tested wind tunnel case in transonic flow conditions. The results obtained have been favourably compared to those measured during the referenced experimental campaign. The strategy was then used in a real world engineering application as the main component of the overall propeller optimization problem, where a surrogate method based on the DoE method was used in order to increase the weighted sum of efficiencies at two different flight regimes by 4.0%.

The main advantage of the proposed technique with respect to other standard approaches is that the modal parameterization has to be built only once. Embedding the structural modes of deformable parts directly into the computational model enables an immediate application of deformation to the CFD grid during the calculation stage.

Finally, the proposed FSI approach represents a universal procedure that can be exploited regardless of the CFD and FEM solver choice, it can be extended to very large models where RBF Morph™ has already proven its computational time efficiency and it is applicable to both steady and unsteady aeroelastic studies.

## ACKNOWLEDGMENT

This work was developed in the framework of the RBF4AERO "Innovative benchmark technology for aircraft engineering design and efficient design phase optimisation" project funded in the Aeronautics and Air Transport (AAT) research thematic area of the EUs 7th Framework Programme (FP7- AAT, 2007-2013) under Grant Agreement no. 605396.

## REFERENCES

- [1] H.J. Bungartz, M. Schäfer, *Fluid-structure interaction: Modeling, simulation, optimization*, Springer-Verlag, 2006.
- [2] H. Gene, W. Jin, L. Anita, Numerical methods for fluid-structure interaction – A review, *Communications in Computational Physics*, 12(2):337-377, 2012.
- [3] Y. Bazilevs, K. Takizawa, T.E. Tezduyar, *Computational fluid-structure interaction: Methods and applications*, Wiley, 2013.
- [4] S. Keye, Fluid-structure coupled analysis of a transport aircraft and comparison to flight data. In *AIAA Paper 2009-4198, 39<sup>th</sup> AIAA Fluid Dynamics Conference*, San Antonio, Texas, USA, June 22-25, 2009.
- [5] M.E. Biancolini, C. Groth, E. Costa, F. Lagasco, A mesh morphing based technique to efficiently perform FSI analyses for aeroelastic design applications, *AIDAA Italian Association of Aeronautics and Astronautics XXII Conference*, Napoli, Italy, September 9-12, 2013.
- [6] S. Jakobsson, O. Amoignon, Mesh deformation using radial basis function for gradient based aerodynamic shape optimization, *Computers and Fluids*, 36(6):1119-1136, 2007.
- [7] A. de Boer, M.S. van der Schoot, H. Bijl, Mesh deformation based on radial basis function interpolation, *Computers and Structures*, 85(11-14):784-795, 2007.
- [8] A.H. van Zuijlen, A. de Boer, H. Bijl, Higher-order time integration through smooth mesh deformation for 3D fluid-structure interaction simulations, *Journal of Computational Physics*, 224:414-430, 2007.
- [9] M.E. Biancolini, U. Cella, An advanced RBF Morph application: coupled CFD-CSM aeroelastic analysis of a full aircraft model and comparison to experimental data, *8<sup>th</sup> MIRA International Vehicle Aerodynamics Conference*, Grove, UK, October 13-14, 2010.
- [10] M.E. Biancolini, C. Groth, An efficient approach to simulating ice accretion on 2D and 3D airfoils, *Advanced Aero Concepts, Design and Operations Conferenc*, Bristol, UK, July 22, 2014.

- 
- [11] E.M. Papoutsis-Kiachagias, M. Andrejašič, S. Porziani, C. Groth, D. Eržen, M.E. Biancolini, E. Costa, K.C. Giannakoglou, Combining an rbf-based morpher with continuous adjoint for low-speed aeronautical optimization applications. In *ECCOMAS Congress 2016, VII European Congress on Computational Methods in Applied Sciences and Engineering*, Crete, Greece, June 5-10, 2016.
- [12] D.H. Kapsoulis, V.G. Asouti, K.C. Giannakoglou, E. Costa, S. Porziani, C. Groth, U. Cella, M.E. Biancolini, Evolutionary aerodynamic shape optimization through the RBF4AERO platform. In *ECCOMAS Congress 2016, VII European Congress on Computational Methods in Applied Sciences and Engineering*, Crete, Greece, June 5-10, 2016.
- [13] M.E. Biancolini, Fluid structure interaction (FSI) with RBF Morph: a generic Formula 1 front end, *EnginSoft International Conference 2011 - CAE Technologies for Industry*, Verona, Italy, October 20-21, 2011.
- [14] M.E. Biancolini, I.M. Viola, M. Riotte, Sails trim optimisation using CFD and RBF mesh morphing, *Computers and Fluids*, 93:46-60, April 10, 2014.  
doi:10.1016/j.compfluid.2014.01.007
- [15] S.G. Kelly, *Mechanical vibrations: theory and applications*, Cengage Learning, 2012.
- [16] R.D. Cook, D.S. Malkus, M.E. Plesha, R.J. Witt, *Concepts and applications of finite element analysis, 4<sup>th</sup> Edition*, John Wiley and Sons, 2002.
- [17] L. Meirovitch, *Fundamentals of vibrations, Reissue edition*, Waveland Press, Inc., 2010.
- [18] C. Micchelli, Interpolation of scattered data: Distance matrices and conditionally positive definite functions, *Constructive Approximation*, 2(1):11–22, 1986.
- [19] A. Beckert, H. Wendland, Multivariate interpolation for fluid-structure interaction problems using radial basis functions, *Aerospace Science and Technology*, 5(2):125–134, 2011.
- [20] U. Cella, M.E. Biancolini, Aeroelastic analysis of aircraft wind-tunnel model coupling structural and fluid dynamic codes, *Journal of Aircraft*, 49(2), 2012.
- [21] AIAA Aeroelastic Prediction Workshop at [https://c3.nasa.gov/dashlink/static/media/other/AEPW\\_legacy.htm](https://c3.nasa.gov/dashlink/static/media/other/AEPW_legacy.htm), (25.2.2016)
- [22] J. Ballmann, A. Boucke, L. Reimer, C. Dickopp, Results of dynamic experiments in the HIRENASD project and analysis of observed unsteady processes, In *IFASD Paper 2009-103, International Forum on Aeroelasticity and Structural Dynamics*, Seattle, USA, 2009.
- [23] P. Chwalowski, J.P. Florance, J. Heeg, C.D. Wieseman, B.P. Perry, Preliminary computational analysis of the HIRENASD configuration in preparation for the aeroelastic prediction workshop, In *IFASD Paper 2011-108, International Forum on Aeroelasticity and Structural Dynamics*, Paris, France, 2011